Reversible regulation of thermal conductivity through spin-crossover transitions

Qichen Song[1], Rahil Ukani[1], Vidhya M. Dev[1], Hong Ki Kim[1], Jungwoo Shin[2], Jinyoung Seo[1], Caleb Stamper[3,4], Daniel W. Laorenza[1], Ryan D. McGillicuddy[1], Jason J. Calvin[1], Yukyung Moon[1], Catherine Thai[1], Jason D. Braun[1], Dehong Yu[4], Gang Chen[2], Jarad A. Mason[1]*

[1]Department of Chemistry and Chemical Biology, Harvard University, Cambridge, MA 02138, USA
[2]Department of Mechanical Engineering, Massachusetts Institute of Technology, Cambridge, MA 02139, USA
[3]Institute for Superconducting and Electronic Materials, University of Wollongong, Wollongong, NSW 2500, Australia
[4]Australian Nuclear Science and Technology Organisation, Lucas Heights, NSW 2234, Australia

Abstract

The development of strategies to modulate the thermal conductivity of a solid in response to an external stimulus is critical to the creation of high-performance thermal regulators, thermal switches, and thermal diodes—devices which would be enabling for a wide range of emerging technologies. Here, we report a new mechanism for achieving switchable solid-state thermal conductivity through a first-order spin-crossover phase transition. Specifically, we show that single crystals of the molecular spin-crossover complex $Fe[HB(tz)_3]_2$ [$HB(tz)_3^-$ = hydrotris(1,2,4-triazol-1-yl)borate] exhibit a large drop in thermal conductivity—more than four-fold—across an electronic spin transition. This thermal conductivity change is highly reversible and can be attributed to lower group velocities of heat-carrying phonons and increased phonon scattering in the high-spin phase of the compound as a result of weaker metal–ligand bonds. We further demonstrate the generalizability of this phenomenon by showing a similarly large change in thermal conductivity for another Fe(II) spin-crossover material with a different coordination environment and transition temperature. Owing to the large structural and chemical diversity of spin-crossover materials and the rich variety of stimuli that can induce electronic spin transitions, these results establish a powerful approach to manipulating thermal transport within solid materials.

*mason@chemistry.harvard.edu

Main

Phase transitions often lead to large changes in the internal properties of a material in response to a small change in the external environment. A high contrast in the properties that can be reversibly accessed when switching between two phases is an enabling feature of phase-change materials for many applications. Though changes to free energy, density, and electronic, magnetic, optical, and mechanical properties have been well studied across a diverse range of solid-state phase transitions, much remains to be understood about how phase transitions impact thermal conductivity[1]. This represents an important knowledge gap since the ability to modulate thermal transport within a solid material is critical to realizing next-generation thermal devices—such as thermal switches[2,3], thermal diodes[4], and thermal regulators[5]—that would provide new opportunities for more efficient and higher performance heat management[6], solid-state cooling[7], and thermal energy storage[8,9] technologies.

Several types of phase transitions—including martensitic transitions[10], amorphous-crystalline transitions[11], rotational transitions[12,13], conformational transitions[14], and metal-insulator transitions[15,16]—have been shown to be accompanied by changes in thermal conductivity, but the library of materials for which thermal conductivity changes have been measured across a phase transition is modest in scope and lacking in structural and chemical diversity. Moreover, challenges associated with low switching ratios, poor reversibility, large hysteresis, slow response times, inconsistent experimental data, and large volume changes that can lead to functional fatigue have made it difficult to implement phase-change materials in functional thermal devices[17–19]. This is particularly true for thermally induced phase transitions, which are important for passive thermal regulation[20].

In pursuit of a phase-change mechanism capable of inducing large thermal conductivity changes without large changes to the internal structure and composition of a material—in order to promote reversibility and fast kinetics—we were drawn to electronic spin-crossover transitions. Spin-crossover (SCO) transitions occur when the ground-state electronic configuration of a molecule or material—most commonly composed of Fe(II) centers bound to N-donor organic ligands—switches between a low-spin (LS) and high-spin (HS) state. This switching arises when the free energy difference between the two states is small because of a balance between the energy difference between valence d orbitals—as dictated by the ligand field—and the energy required to pair two electrons in the same orbital. In such a case, enthalpic effects drive the system to an LS configuration at low temperatures, and entropic effects drive a transition to a HS configuration at higher temperatures.

The entropic driving force for a SCO transition arises both from an increase in electronic entropy due to the presence of more unpaired electrons in the HS state [13.4 J mol^{-1} K^{-1} for d^6 Fe(II)] and from an increase in phonon (vibrational) entropy as electrons populate metal–ligand molecular orbitals that have greater anti-bonding character. Phonon entropy is usually the predominant contribution[21,22], and the associated anti-bonding orbital occupation is also responsible for the weakening of metal–ligand bonds that accompanies most SCO transitions. We hypothesized that this bond weakening could have a large effect on thermal transport within an SCO material by softening the crystal lattice and altering the phonon density of states. Indeed, the spin state of Fe centers has been shown to impact the thermal conductivity of the Earth's lower mantle[23] and certain molecular Fe(III) complexes[24]. To the best of our knowledge, however, there have not been any reports of thermal conductivity changes across a discrete first-order SCO phase transition in a material.

In order to begin investigating the impact of a first-order SCO transition on thermal conductivity, we sought a SCO material with 1) a sharp transition between a single low-spin and single high-spin state, 2) minimal thermal hysteresis, 3) no spectator charge-balancing ions, and 4) a compact ligand scaffold. Though there are many compounds that could satisfy these criteria, we selected the Fe(II)-based molecular coordination complex $Fe[HB(tz)_3]_2$ [$HB(tz)_3^-$ = hydrotris(1,2,4-triazol-1-yl)borate] as a particularly well-suited initial candidate for switchable thermal conductivity across a SCO transition[25]. This neutral, mononuclear complex consists of an Fe(II) center bound to two tridentate, anionic organic ligands in a trigonal antiprismatic coordination geometry (D_{3d} symmetry). In the solid state, $Fe[HB(tz)_3]_2$ crystallizes into an orthorhombic lattice[26] held together through a combination of weak hydrogen bonding and van der Waals interactions between complexes (Fig. 1a). As has been previously reported[27], the compound undergoes a highly cooperative SCO transition at 332 K between a singlet (S = 0) state at low temperatures and a quintet (S = 2) state at high temperatures (Figs. 1b, 1c, and 1e). This transition is accompanied by an overall volume expansion of 3.6% that arises from an average increase in Fe–N bond lengths of 0.16 Å (8%), but the SCO transition does not lead to any changes to the lattice structure of the material or the relative orientation of individual complexes. Notably, this SCO transition is highly reversible with a thermal hysteresis of less than 1 K and negligible changes to the phase-change properties even after ten million thermal cycles[28].

To assess the impact of the SCO transition on thermal transport, we used frequency-domain thermoreflectance (FDTR) to measure the thermal conductivity of individual single crystals of $Fe[HB(tz)_3]_2$ as a function of temperature. Specifically, a continuous-wave (CW) pump laser (λ = 458 nm) was modulated at a certain frequency and used to heat the sample periodically (Fig. 1f)[29,30]. A thin-film (93 nm) Au transducer layer was deposited on $Fe[HB(tz)_3]_2$ crystals in order to convert the energy of the photons from the pump laser into heat. The temperature oscillations at the surface of the metal transducer were then measured through the thermoreflectance of a probe laser beam (λ = 532 nm). The temperature modulations at the surface have a phase lag with respect to the phase of the pump heating power that is related to the thermal conductivity of the underlying sample, along with the sample heat capacity and the thermal boundary conductance between the transducer and sample. Compared to traditional techniques for measuring the thermal conductivity of macroscopic samples, FDTR offers the advantage of providing a direct probe of the intrinsic thermal conductivity within a material, without complications from interparticle heat transfer inherent in the pellet sample geometry[31].

It is immediately clear from the raw FDTR data that the phase lag for $Fe[HB(tz)_3]_2$ abruptly increases after the SCO transition from the LS to HS phase over a modulation frequency range of 0.8 MHz to 30 MHz (Fig. 1g), which suggests a sudden drop in thermal conductivity. By fitting the FDTR data with a Fourier heat conduction model and independently measuring the temperature dependence of the heat capacity of $Fe[HB(tz)_3]_2$ (Fig. 1d) (see Supplementary Information for details), the thermal conductivity of $Fe[HB(tz)_3]_2$ was extracted and found to exhibit a large drop across the SCO transition, from 0.70 W m^{-1} K^{-1} (323 K) in the LS phase to 0.16 W m^{-1} K^{-1} (340 K) in the HS phase (Fig. 1h). To further validate these results, we performed FDTR measurements on two different instruments, several different $Fe[HB(tz)_3]_2$ single crystals, multiple regions of each single crystal, and a $Fe[HB(tz)_3]_2$ crystal coated with a lower-conductivity $Au_{0.93}Ti_{0.07}$ alloy transducer layer instead of a pure Au layer, observing similar thermal conductivity changes in all cases (Fig. S6). To evaluate the reversibility of this thermal conductivity switching, we heated and cooled an individual $Fe[HB(tz)_3]_2$ single crystal through the SCO transition 30 times (Fig. 2a). The phase lags and thermal conductivities of the LS and HS phases were very consistent during each cycle, as was the switching behavior.

The change in thermal conductivity that $Fe[HB(tz)_3]_2$ experiences as a result of the SCO transition is remarkable, particularly considering that it occurs over such a narrow temperature range (< 20 K) and involves such a small structural change (< 0.2 Å increase in Fe–N bond lengths). Indeed, the thermal conductivity switching ratio for $Fe[HB(tz)_3]_2$ exceeds those reported for other thermal phase-change materials (Fig. 2b), including ones that undergo solid-liquid melting transitions ($Ge_2Sb_2Te_5$, Hg, H_2O, $CaCl_2{\cdot}6H_2O$, $Ba(OH)_2{\cdot}8H_2O$, $MgCl_2{\cdot}6H_2O$ and paraffin wax)[32–34], structural transitions (Ni-Mn-In[10], C_{60}[12], and $[Co_6Se_8][C_{60}]_2$[13]), and metal-insulator transitions (a VO_2 thin film[15] and nanowire[16]). While crystalline polyethylene nanofibers can exhibit a high switching ratio, they are excluded from our comparison due to the proximity of the structural phase transition to the melting temperature, which compromises the reversibility and operating range of the materials.

We sought to gain additional insight into the microscopic origins of the large thermal conductivity contrast in $Fe[HB(tz)_3]_2$ through a combination of inelastic neutron scattering experiments, Raman scattering experiments, and quantum mechanical simulations. With a low electrical conductivity ($<10^{-6}$ S/m)[35], heat within $Fe[HB(tz)_3]_2$ will be primarily conducted through lattice vibrations (phonons)—the properties of which will be impacted by the SCO transition and can be directly probed by inelastic neutron scattering[36]. Specifically, the generalized phonon density of states is given by $\mathrm{GDOS}(\omega) = \int g(Q,\omega)dQ$, where $g(Q,\omega)$ is the normalized inelastic neutron scattering function, given by $g(Q,\omega) = \frac{\omega}{(n(\omega,T)+1)Q^2}S(Q,\omega)$. Here, $n(\omega,T)$ is the Bose-Einstein distribution function, and $S(Q,\omega)$ is the dynamic neutron scattering function of the sample at the momentum transfer $\hbar Q$ and phonon frequency ω, which is normalized to ensure $\int \mathrm{GDOS}(\omega) = 3N/V$, where N is the number of atoms in the unit cell and V is the volume of the unit cell. As depicted in Figs. 3a and 3b, we observe clear changes to the normalized inelastic neutron scattering function during the SCO transition. Notably, two shallow gaps between the phonon bands centered at 2.7 THz, 4.3 THz, and 5.9 THz disappear in the HS phase as these bands all shift to lower energies. The disappearance of these shallow gaps should allow for more three-phonon scattering processes to occur by making it easier to satisfy energy conservation, which would contribute to decreasing thermal conductivity. By evaluating the three-phonon scattering phase space (Eq. S42), we estimate a decrease in phonon lifetime by a factor of at least 1.5 across the SCO transition for phonons below 4 THz (Fig. 3h).

The GDOS for $Fe[HB(tz)_3]_2$ shows that phonon bands below 12 THz experience a substantial softening (decrease in frequency) during the transition from the LS to HS phase (Fig. 3c). For example, the optical phonon peak at 5.9 THz shifts to 4.8 THz, and the optical phonon peak at 4.3 THz shifts to 3.0 THz. On average, the frequencies of optical phonon peaks between 4 THz and 8 THz decrease by a factor of $\left(\frac{\omega_{\mathrm{LS}}}{\omega_{\mathrm{HS}}}\right)^2 = 1.6$ during the SCO transition (Fig. 3d), which directly leads to a reduction in the off-diagonal element of the group velocity matrix, v_{ij}, that is responsible for heat transfer via wave-like phonon tunneling[37,38] by a factor of $\left(\frac{v_{\mathrm{LS},ij}}{v_{\mathrm{HS},ij}}\right)^2 \approx \left(\frac{\omega_{\mathrm{LS}}}{\omega_{\mathrm{HS}}}\right)^2$ (Fig. S7). In addition, the GDOS shows minimal variation with temperature within each spin state, highlighting that the changes in phonon properties can be attributed to the SCO transition rather than to a temperature effect. Consistently, the hydrogen-projected phonon density of states from density functional tight-binding calculations, which is directly related to the GDOS because of the abundant hydrogen atoms in the lattice, exhibits marked red shifts for optical phonon peaks below 12 THz across the SCO transition (Fig. 3f). The prominent peak in the vibrational spectra measured by Stokes Raman scattering also aligns well with that in the GDOS obtained from inelastic neutron scattering (Fig. 3g). Importantly, the suppression of the high-frequency modes and promotion of the low-frequency modes provide additional support for optical phonon softening across the SCO transition.

The group velocity, v, of the acoustic phonons, which can be extracted by fitting the low-energy GDOS according to the scaling relation $\mathrm{GDOS}(\omega) \approx \frac{3\omega^2}{2\pi^2 v^3}$, decreases substantially from the LS phase at 300 K to the HS phase at 350 K with $\left(\frac{v_{\mathrm{LS}}}{v_{\mathrm{HS}}}\right)^2 = 1.5$ (Fig. 3e). This decreased phonon velocity will suppress thermal conductivity due to particle-like phonon transport by the same factor. The reduction in group velocity is also in good agreement with that observed in the Fe partial vibrational density of states determined by resonant nuclear inelastic scattering[39]. Moreover, nanoindentation measurements suggest a group velocity decrease from 2432 m/s at 318 K to 1755 m/s at 343 K with $\left(\frac{v_{\mathrm{LS}}}{v_{\mathrm{HS}}}\right)^2 = 1.9$ (Fig. S24). Though both inelastic neutron scattering and nanoindentation experiments show that the SCO transition has the same effect on group velocity, differences in the magnitude of the decrease determined by each technique may be the result of the anisotropic nature of the SCO transition in $Fe[HB(tz)_3]_2$, for which the structural expansion occurs preferentially along the crystallographic c axis. Regardless, the observed redshifts of phonon frequencies and reduction in acoustic phonon velocities directly contribute to the reduction in thermal conductivity of $Fe[HB(tz)_3]_2$ after the SCO transition.

To better understand the origins of phonon softening at a molecular level, we studied the lattice dynamics in $Fe[HB(tz)_3]_2$ using quantum mechanical simulations. Since it is challenging to directly compute the interatomic force constants at the density-functional-theory (DFT) level—as there are 188 atoms in the primitive unit cell—we used the density functional tight-binding (DFTB) method. The relaxed atomic structures of both the LS and HS phases calculated using DFTB are in good agreement with the experimental single crystal structures (Fig. S26). As Fe–N bond lengths increase during the SCO transition, the force constants $\Psi_{ij}^{\alpha=\beta}$ for Fe atom i and N atom j moving along the same Cartesian axis decrease by a factor of 2 to 4 (Fig. 4a). These weaker bonds favor softer phonons, as the magnitudes of the force constants, $|\Psi_{ij}^{\alpha\beta}|$, scale with the phonon frequency squared, ω^2. Hydrogen bonding interactions between molecular complexes also show a modest decrease in their absolute force constants as the average hydrogen bond length slightly elongates (by <1%) during the SCO transition (Fig. 4b). Since intramolecular and intermolecular bonding collectively determine the lattice dynamics, the square of the ratio between phonon frequencies at the Γ point (the center of the 1st Brillouin zone) in the LS and HS phases $[(\omega_{\mathrm{LS}}/\omega_{\mathrm{HS}})^2]$ decreases as the phonon frequency of the LS phase (ω_{LS}) increases (Fig. 4c), and the highest value is above 1.9. This is consistent with the phonon softening observed by inelastic neutron scattering, nanoindentation and Raman scattering. Moreover, the phonon polarization vectors experience subtle changes from the LS to HS phase (Fig. 4e), as reflected in the increased amplitudes of hydrogen-bond librations—angular bond oscillations that are intrinsically softer than bond-stretching vibrations (Fig. S29).

To evaluate the relative contributions of intramolecular and intermolecular interactions to lattice vibrations, we defined a mode-resolved metric, $\eta_\lambda = \frac{\mathbf{u}_\lambda^\dagger \mathbf{D}_{\mathrm{inter}} \mathbf{u}_\lambda}{\mathbf{u}_\lambda^\dagger (\mathbf{D}_{\mathrm{inter}} + \mathbf{D}_{\mathrm{intra}}) \mathbf{u}_\lambda}$, as the ratio between the vibrational energy associated with intermolecular interactions and the total vibrational energy in the unit cell. Here, $\mathbf{D}_{\mathrm{inter}}$ and $\mathbf{D}_{\mathrm{intra}}$ are dynamical matrices constructed at the Γ point using the calculated intermolecular and intramolecular force constants, respectively, and $\mathbf{u}_\lambda$ is the eigenvector of phonon mode λ (see Supplementary Information for more detail). In both spin states, phonons possess less intermolecular character with increasing frequency (Fig. 4d). This suggests that more intramolecular bonds are involved in higher frequency phonons, increasing the relative importance of $\mathbf{D}_{\mathrm{intra}}$ compared to $\mathbf{D}_{\mathrm{inter}}$. At lower frequencies, optical phonon modes with $\eta_\lambda >$ 80% are present in the HS state but not the LS states, which is another manifestation of phonon softening because of weakened intramolecular interactions ($\mathbf{D}_{\mathrm{intra}}$). Overall, our calculations reveal that changes in bond strengths and in specific vibrational features—particularly the contribution of librational modes—rather than structural and symmetry variations, are responsible for the softening of the entire lattice.

To establish the generalizability of SCO-induced thermal switching , we synthesized single crystals of the neutral complex $Fe(Fpr\text{-}trz_2\text{-}dmpn)(NCS)_2$ [$Fpr\text{-}trz_2\text{-}dmpn$ = bis[(1-(3-fluoropropyl)-1H-1,2,3-triazol-4-yl)methylene]-2,2-dimethylpropane-1,3-diamine] (Fig. 5a), which undergoes a sharp SCO transition near 270 K with minimal associated thermal hysteresis (Fig. 5b)[40]. Phonon entropy, arising from changes in lattice dynamics, is the primary driver of the SCO transition, as in $Fe[HB(tz)_3]_2$ (Fig. 5c). The variable temperature heat capacity of the single crystals, as measured by differential scanning calorimetry (DSC), shows an expected peak associated with the SCO transition at $T_{tr} = 266$ K (Fig. 5d). We then deposited the single crystals on a Si substrate and coated them with a thin-film Au layer for FDTR measurements. Similar to $Fe[HB(tz)_3]_2$, we observed substantially larger phase lags in the HS phase of $Fe(Fpr\text{-}trz_2\text{-}dmpn)(NCS)_2$ than in the LS phase, which results in a pronounced thermal conductivity switching ratio of 3.3 across the SCO transition (Fig. 5e,f). Interestingly, the thermal conductivities of LS and HS phases of $Fe(Fpr\text{-}trz_2\text{-}dmpn)(NCS)_2$ are both substantially lower than those of $Fe[HB(tz)_3]_2$. This can be attributed to the reduced molecular symmetry (C_1 rather than D_{3d}), lower-symmetry crystal structure ($P2_1/c$ rather than Pbca), and more conformationally flexible ligand shell for the former compound, which intrinsically impose fewer constraints on three-phonon scattering processes and thus shortens the phonon lifetimes. Nevertheless, the clear contrast between the thermal conductivity of the LS and HS phases persists, highlighting that efficient thermal switching can be achieved via SCO transitions in compounds with very different structures and compositions.

The foregoing results demonstrate that electronic spin-state transitions in coordination complexes can lead to large, reversible changes in the thermal conductivity of a solid material over a narrow temperature range. Unlike most approaches to thermal conductivity switching that rely primarily on tuning the phonon scattering lifetime (anharmonicity) through large structural changes, the SCO transition directly modulates the phonon group velocity through small changes to metal–ligand bond lengths. The small volume change that accompanies these changes should simplify the fabrication of thermal devices. Moreover, there are myriad possibilities for manipulating SCO materials through ligand design, including the ability to synthesize compounds that are connected by 1-, 2-, or 3-D networks of coordination bonds. In addition to temperature, SCO transitions can also be induced by hydrostatic pressure[41] and, in some cases, light[42], a voltage bias[43], an applied magnetic field[44], or uptake of guest molecules[45]. This tunability and sensitivity to a range of external stimuli provides a vast design space for leveraging SCO transitions to manipulate thermal transport.

References

1. Chen, H. *et al.* Thermal conductivity during phase transitions. *Adv. Mater.* **31**, 1806518 (2019).

2. Lu, Q. *et al.* Bi-directional tuning of thermal transport in $SrCoO_x$ with electrochemically induced phase transitions. *Nat. Mater.* **19**, 655–662 (2020).

3. Li, M. *et al.* Electrically gated molecular thermal switch. *Science* **382**, 585–589 (2023).

4. Chang, C. W., Okawa, D., Majumdar, A. & Zettl, A. Solid-state thermal rectifier. *Science* **314**, 1121–1124 (2006).

5. Zheng, R., Gao, J., Wang, J. & Chen, G. Reversible temperature regulation of electrical and thermal conductivity using liquid–solid phase transitions. *Nat. Commun.* **2**, 1–6 (2011).

6. Browne, M. C., Norton, B. & McCormack, S. J. Phase change materials for photovoltaic thermal management. *Renew. Sustain. Energy Rev.* **47**, 762–782 (2015).

7. Klinar, K. & Kitanovski, A. Thermal control elements for caloric energy conversion. *Renew. Sustain. Energy Rev.* **118**, 109571 (2020).

8. Gur, I., Sawyer, K. & Prasher, R. Searching for a better thermal battery. *Science* **335**, 1454–1455 (2012).

9. Usman, A., Xiong, F., Aftab, W., Qin, M. & Zou, R. Emerging solid-to-solid phase-change materials for thermal-energy harvesting, storage, and utilization. *Adv. Mater.* **34**, 2202457 (2022).

10. Zheng, Q., Zhu, G., Diao, Z., Banerjee, D. & Cahill, D. G. High contrast thermal conductivity change in Ni–Mn–In Heusler alloys near room temperature. *Adv. Eng. Mater.* **21**, 1801342 (2019).

11. Lyeo, H. K. *et al.* Thermal conductivity of phase-change material $Ge_2Sb_2Te_5$. *Appl. Phys. Lett.* **89**, 151904 (2006).

12. Yu, R. C., Tea, N., Salamon, M. B., Lorents, D. & Malhotra, R. Thermal conductivity of single crystal C_{60}. *Phys. Rev. Lett.* **68**, 2050–2053 (1992).

13. Ong, W. L. *et al.* Orientational order controls crystalline and amorphous thermal transport in superatomic crystals. *Nat. Mater.* **16**, 83–88 (2016).

14. Shin, J. *et al.* Light-triggered thermal conductivity switching in azobenzene polymers. *Proc. Natl. Acad. Sci. U. S. A.* **116**, 5973–5978 (2019).

15. Oh, D. W., Ko, C., Ramanathan, S. & Cahill, D. G. Thermal conductivity and dynamic heat capacity across the metal-insulator transition in thin film VO_2. *Appl. Phys. Lett.* **96**, 151906 (2010).

16. Lee, S. *et al.* Anomalously low electronic thermal conductivity in metallic vanadium dioxide. *Science* **355**, 371–374 (2021).

17. Yuan, K. *et al.* Engineering the thermal conductivity of functional phase-change materials for heat energy conversion, storage, and utilization. *Adv. Funct. Mater.* **30**, 1904228 (2020).

18. Li, Y. *et al.* Transforming heat transfer with thermal metamaterials and devices. *Nat. Rev. Mater.* **6**, 488–507 (2021).

19. Swoboda, T., Klinar, K., Yalamarthy, A. S., Kitanovski, A. & Muñoz Rojo, M. Solid-state thermal control devices. *Adv. Electron. Mater.* **7**, 2000625 (2021).

20. Wehmeyer, G., Yabuki, T., Monachon, C., Wu, J. & Dames, C. Thermal diodes, regulators, and switches: Physical mechanisms and potential applications. *Appl. Phys. Rev.* **4**, 41304 (2017).

21. Bousseksou, A. *et al.* Raman spectroscopy of the high- and low-spin states of the spin crossover complex $Fe(phen)_2(NCS)_2$: An initial approach to estimation of vibrational contributions to the associated entropy change. *Chem. Phys. Lett.* **318**, 409–416 (2000).

22. Brehm, G., Reiher, M. & Schneider, S. Estimation of the vibrational contribution to the entropy change associated with the low- to high-spin transition in $Fe(phen)_2(NCS)_2$ complexes: Results obtained by IR and Raman spectroscopy and DFT calculations. *J. Phys. Chem. A* **106**, 12024–12034 (2002).

23. Hsieh, W. P., Deschamps, F., Okuchi, T. & Lin, J. F. Effects of iron on the lattice thermal conductivity of Earth's deep mantle and implications for mantle dynamics. *Proc. Natl. Acad. Sci. U. S. A.* **115**, 4099–4104 (2018).

24. Hoshino, N., Hayashi, A. & Akutagawa, T. The strong correlations between thermal conductivities and electronic spin states in the crystals of Fe(III) spin crossover complexes. *Dalt. Trans.* **51**, 12698–12703 (2022).

25. Janiak, C. *et al.* Effects of nitrogen substitution in poly(pyrazolyl)borato ligands: from orbital energy levels to C–H···O hydrogen bonding. *Chem. – A Eur. J.* **2**, 992–1000 (1996).

26. Rat, S. *et al.* Solvatomorphism and structural-spin crossover property relationship in bis[hydrotris(1,2,4-triazol-1-yl)borate]iron(II). *CrystEngComm* **19**, 3271–3280 (2017).

27. van Koningsbruggen, P. J. & Miller, J. S. Observation of a 331 K (58 °C) spin transition for bis[hydrotris(1,2,4-triazol-1-yl)borate]iron(II) by variable temperature infrared spectroscopy and magnetic susceptibility measurements. *Solid State Sci.* **10**, 1804–1806 (2008).

28. Ridier, K. *et al.* Unprecedented switching endurance affords for high-resolution surface temperature mapping using a spin-crossover film. *Nat. Commun.* **11**, 1–9 (2020).

29. Schmidt, A. J., Cheaito, R. & Chiesa, M. A frequency-domain thermoreflectance method for the characterization of thermal properties. *Rev. Sci. Instrum.* **80**, 094901 (2009).

30. Yang, J., Ziade, E. & Schmidt, A. J. Modeling optical absorption for thermoreflectance measurements. *J. Appl. Phys.* **119**, 095107 (2016).

31. Olson, D. H., Braun, J. L. & Hopkins, P. E. Spatially resolved thermoreflectance techniques for thermal conductivity measurements from the nanoscale to the mesoscale. *J. Appl. Phys.* **126**, 150901 (2019).

32. Crespi, L., Ghetti, A., Boniardi, M. & Lacaita, A. L. Electrical conductivity discontinuity at melt in phase change memory. *IEEE Electron Device Lett.* **35**, 747–749 (2014).

33. Ho, C. Y., Powell, R. W. & Liley, P. E. Thermal conductivity of the elements. *J. Phys. Chem. Ref. Data* **1**, 279–421 (1972).

34. Lane, G. A. Low temperature heat storage with phase change materials. *Int. J. Ambient Energy* **1**, 155–168 (1980).

35. Zhang, Y. *et al.* Switching endurance of the molecular spin crossover complex [Fe(HB(tz)$_3$)$_2$]: from single crystals to thin films and electronic devices. *Mater. Adv.* **3**, 8193–8200 (2022).

36. Furrer, A., Mesot, J. & Strässle, T. Neutron scattering in condensed matter physics. *Neutron Scatt. Condens. Matter Phys.* 1–317 (2009).

37. Simoncelli, M., Marzari, N. & Mauri, F. Unified theory of thermal transport in crystals and glasses. *Nat. Phys.* **15**, 809–813 (2019).

38. Isaeva, L., Barbalinardo, G., Donadio, D. & Baroni, S. Modeling heat transport in crystals and glasses from a unified lattice-dynamical approach. *Nat. Commun.* **10**, 1–6 (2019).

39. Mikolasek, M. *et al.* Complete set of elastic moduli of a spin-crossover solid: spin-state dependence and mechanical actuation. *J. Am. Chem. Soc.* **140**, 8970–8979 (2018).

40. Seredyuk, M. *et al.* Reversible colossal barocaloric effect of a new Fe^{II} molecular complex with low hysteretic spin crossover behavior. *Adv. Funct. Mater.* **34**, 2315487 (2024).

41. Seo, J., Braun, J. D., Dev, V. M. & Mason, J. A. Driving barocaloric effects in a molecular spin-crossover complex at low pressures. *J. Am. Chem. Soc.* **144**, 6493–6503 (2022).

42. Chastanet, G., Lorenc, M., Bertoni, R. & Desplanches, C. Light-induced spin crossover—Solution and solid-state processes. *Comptes Rendus Chim.* **21**, 1075–1094 (2018).

43. Osorio, E. A. *et al.* Electrical manipulation of spin states in a single electrostatically gated transition-metal complex. *Nano Lett.* **10**, 105–110 (2010).

44. Bousseksou, A. *et al.* Dynamic response of the spin-crossover solid Co(H$_2$(fsa)$_2$en)(py)$_2$ to a pulsed magnetic field. *Phys. Rev. B* **65**, 172412 (2002).

45. Halder, G. J., Kepert, C. J., Moubaraki, B., Murray, K. S. & Cashion, J. D. Guest-dependent spin crossover in a nanoporous molecular framework material. *Science* **298**, 1762–1765 (2002).

46. Song, Q., Warkander, S. & Huberman, S. C. Probing carrier and phonon transport in semiconductors all at once through frequency-domain photoreflectance. *Phys. Rev. Appl.* **21**, 034044 (2024).

47. Yang, J., Ziade, E. & Schmidt, A. J. Uncertainty analysis of thermoreflectance

measurements. *Rev. Sci. Instrum.* **87**, 14901 (2016).

48. Dehong, Y., Richard, M., Terry, N., Shane, K. & Robert, R. Pelican — a time of flight cold neutron polarization analysis spectrometer at OPAL. *J. Phys. Soc. Japan* **82**, SA027 (2013).

49. Grimme, S., Bannwarth, C. & Shushkov, P. A robust and accurate tight-binding quantum chemical method for structures, vibrational frequencies, and noncovalent interactions of large molecular systems parametrized for all spd-block elements (Z = 1—86). *J. Chem. Theory Comput.* **13**, 1989–2009 (2017).

50. Shi, Q., Boerio-Goates, J. & Woodfield, B. F. An improved technique for accurate heat capacity measurements on powdered samples using a commercial relaxation calorimeter. *J. Chem. Thermodyn.* **43**, 1263–1269 (2011).

51. Feser, J. P., Liu, J. & Cahill, D. G. Pump-probe measurements of the thermal conductivity tensor for materials lacking in-plane symmetry. *Rev. Sci. Instrum.* **85**, 104903 (2014).

52. Jiang, P., Qian, X. & Yang, R. A new elliptical-beam method based on time-domain thermoreflectance (TDTR) to measure the in-plane anisotropic thermal conductivity and its comparison with the beam-offset method. *Rev. Sci. Instrum.* **89**, 94902 (2018).

53. Tang, L. & Dames, C. Anisotropic thermal conductivity tensor measurements using beam-offset frequency domain thermoreflectance (BO-FDTR) for materials lacking in-plane symmetry. *Int. J. Heat Mass Transf.* **164**, 120600 (2021).

54. Wilson, R. B. & Cahill, D. G. Anisotropic failure of Fourier theory in time-domain thermoreflectance experiments. *Nat. Commun.* **5**, 5075 (2014).

55. Regner, K. T., Wei, L. C. & Malen, J. A. Interpretation of thermoreflectance measurements with a two-temperature model including non-surface heat deposition. *J. Appl. Phys.* **118**, 235101 (2015).

56. Wilson, R. B., Feser, J. P., Hohensee, G. T. & Cahill, D. G. Two-channel model for nonequilibrium thermal transport in pump-probe experiments. *Phys. Rev. B* **88**, 144305 (2013).

57. Wilson, R. B. *et al.* Thermoreflectance of metal transducers for optical pump-probe studies of thermal properties. *Opt. Express* **20**, 28829–28838 (2012).

58. Cahill, D. G. Analysis of heat flow in layered structures for time-domain thermoreflectance. *Rev. Sci. Instrum.* **75**, 5119–5122 (2004).

59. Mathews, J. & Walker, R. L. *Mathematical Methods of Physics*. (W.A. Benjamin, 1970).

60. Carslaw, H. S. & Jaeger, J. C. *Conduction of Heat in Solids*. (Oxford University Press, 1959).

61. Ravichandran, N. K. & Broido, D. Phonon-phonon interactions in strongly bonded solids: selection rules and higher-order processes. *Phys. Rev. X* **10**, 021063 (2020).

62. Ashcroft, N. W. & Mermin, N. D. *Solid State Physics*. (Cengage Learning, 1976).

63. West, D. & Estreicher, S. K. First-principles calculations of vibrational lifetimes and decay channels: hydrogen-related modes in Si. *Phys. Rev. Lett.* **96**, 115504 (2006).

64. Shulumba, N., Hellman, O. & Minnich, A. J. Intrinsic localized mode and low thermal conductivity of PbSe. *Phys. Rev. B* **95**, 14302 (2017).

65. Parr, R. G. & Weitao, Y. *Density-Functional Theory of Atoms and Molecules*. (Oxford University Press, 1994).

66. Bochevarov, A. D. *et al.* Jaguar: A high-performance quantum chemistry software program with strengths in life and materials sciences. *Int. J. Quantum Chem.* **113**, 2110–2142 (2013).

67. Slater, J. C. & Phillips, J. C. *Quantum theory of molecules and solids*. (McGraw Hill, New York, 1974).

68. Vosko, S. H. *et al.* Accurate spin-dependent electron liquid correlation energies for local spin density calculations: a critical analysis. *CaJPh* **59**, 1200 (1980).

69. Becke, A. D. Density-functional exchange-energy approximation with correct asymptotic behavior. *Phys. Rev. A* **38**, 3098 (1988).

70. Lee, C., Yang, W. & Parr, R. G. Development of the Colle-Salvetti correlation-energy formula into a functional of the electron density. *Phys. Rev. B* **37**, 785 (1988).

71. Grimme, S., Antony, J., Ehrlich, S. & Krieg, H. A consistent and accurate ab initio parametrization of density functional dispersion correction (DFT-D) for the 94 elements H—Pu. *J. Chem. Phys.* **132**, 154104 (2010).

72. Ditchfield, R., Hehre, W. J. & Pople, J. A. Self-consistent molecular-orbital methods. IX. An extended Gaussian-type basis for molecular-orbital studies of organic molecules. *J. Chem. Phys.* **54**, 724–728 (1971).

73. Hay, P. J. & Wadt, W. R. *Ab initio* effective core potentials for molecular calculations. Potentials for K to Au including the outermost core orbitals. *J. Chem. Phys.* **82**, 299–310 (1985).

74. Wadt, W. R. & Hay, P. J. *Ab initio* effective core potentials for molecular calculations. Potentials for main group elements Na to Bi. *J. Chem. Phys.* **82**, 284–298 (1985).

75. Hay, P. J. & Wadt, W. R. *Ab initio* effective core potentials for molecular calculations. Potentials for the transition metal atoms Sc to Hg. *J. Chem. Phys.* **82**, 270–283 (1985).

76. Dunning, T. H. Gaussian basis sets for use in correlated molecular calculations. I. The atoms boron through neon and hydrogen. *J. Chem. Phys.* **90**, 1007–1023 (1989).

77. Rashin, A. A. & Honig, B. Reevaluation of the Born model of ion hydration. *J. Phys. Chem.* **89**, 5588–5593 (1985).

78. Zimmermann, R. & König, E. A model for high-spin/low-spin transitions in solids including the effect of lattice vibrations. *J. Phys. Chem. Solids* **38**, 779–788 (1977).

79. Nishino, M., Boukheddaden, K., Konishi, Y. & Miyashita, S. Simple two-dimensional

model for the elastic origin of cooperativity among spin states of spin-crossover complexes. *Phys. Rev. Lett.* **98**, 247203 (2007).

80. Dolomanov, O. V., Bourhis, L. J., Gildea, R. J., Howard, J. A. K. & Puschmann, H. OLEX2: a complete structure solution, refinement and analysis program. *J. Appl. Crystallogr.* **42**, 339–341 (2009).

81. Sheldrick, G. M. SHELXT - integrated space-group and crystal-structure determination. *Acta Crystallogr. Sect. A, Found. Adv.* **71**, 3–8 (2015).

82. Sheldrick, G. M. Crystal structure refinement with SHELXL. *Acta Crystallogr. Sect. C, Struct. Chem.* **71**, 3–8 (2015).

83. Rafizadeh, H. A. & Yip, S. Lattice dynamics of hexamine—a rigid-molecule approximation. *J. Chem. Phys.* **53**, 315–325 (1970).

84. Boča, R. Zero-field splitting in metal complexes. *Coord. Chem. Rev.* **248**, 757–815 (2004).

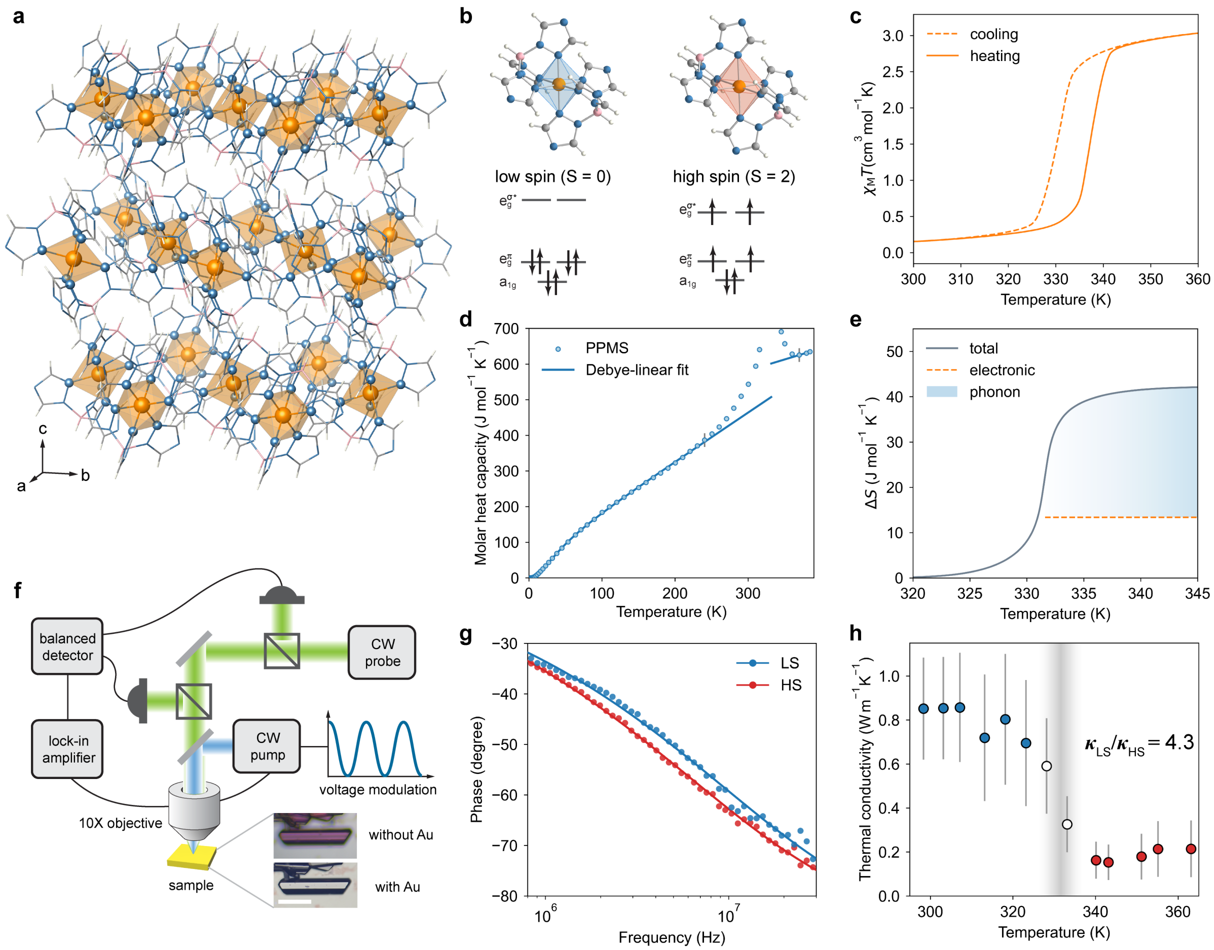

Fig. 1 | Thermal conductivity changes across a spin-crossover phase transition. a, Crystal structure of $Fe[HB(tz)_3]_2$ in the LS phase to illustrate the weak, non-covalent interactions between molecular complexes in the solid state. Orange and blue spheres represent Fe and N atoms, respectively. Grey, blue, white, and pink rods represent C, N, H, and B atoms, respectively. **b**, The atomic structure and valence electronic structure of the LS and HS phases of $Fe[HB(tz)_3]_2$. Grey, blue, white, pink, and orange spheres represent C, N, H, B, and Fe atoms, respectively. **c**, Temperature dependence of the product of magnetic susceptibility and temperature ($\chi_M T$) for $Fe[HB(tz)_3]_2$, highlighting the low hysteresis associated with its spin-crossover transition. **d**, Experimental heat capacity of $Fe[HB(tz)_3]_2$ as measured by a PPMS (blue circles) and a fit (blue line) that combines a Debye model with a linear function of temperature. Temperatures near the phase transition—as indicated by the region marked with vertical lines—are excluded from the model fitting. **e**, The phonon (vibrational) entropy change (shaded region) represents ~71% of the total entropy change (gray line) associated with the SCO transition of $Fe[HB(tz)_3]_2$, with the balance being due to a change in electronic entropy (orange dashed line). **f**, A schematic of the frequency-domain thermoreflectance (FDTR) instrument used to measure the thermal conductivity of single crystals of $Fe[HB(tz)_3]_2$ as a function of temperature. The insets show optical microscope images of a $Fe[HB(tz)_3]_2$ single crystal in the LS phase with and without the gold transducer layer. Scale bar, 100 µm. **g**, The phase lag of the thermoreflectance signal from FDTR measurements (dots) and best fits from a Fourier heat conduction model (lines) are shown for the LS (318 K) and HS (343 K) phase of $Fe[HB(tz)_3]_2$. **h**, The temperature dependence of thermal conductivity for $Fe[HB(tz)_3]_2$ determined from FDTR measurements for a single crystal of $Fe[HB(tz)_3]_2$ in the LS (blue circles) and HS (red circles) phase. The shaded region represents a temperature window of 10 K centered around T_{tr} = 331 K where the two spin phases can coexist. Error bars represent the uncertainty in the best fit, evaluated using Monte Carlo simulations.

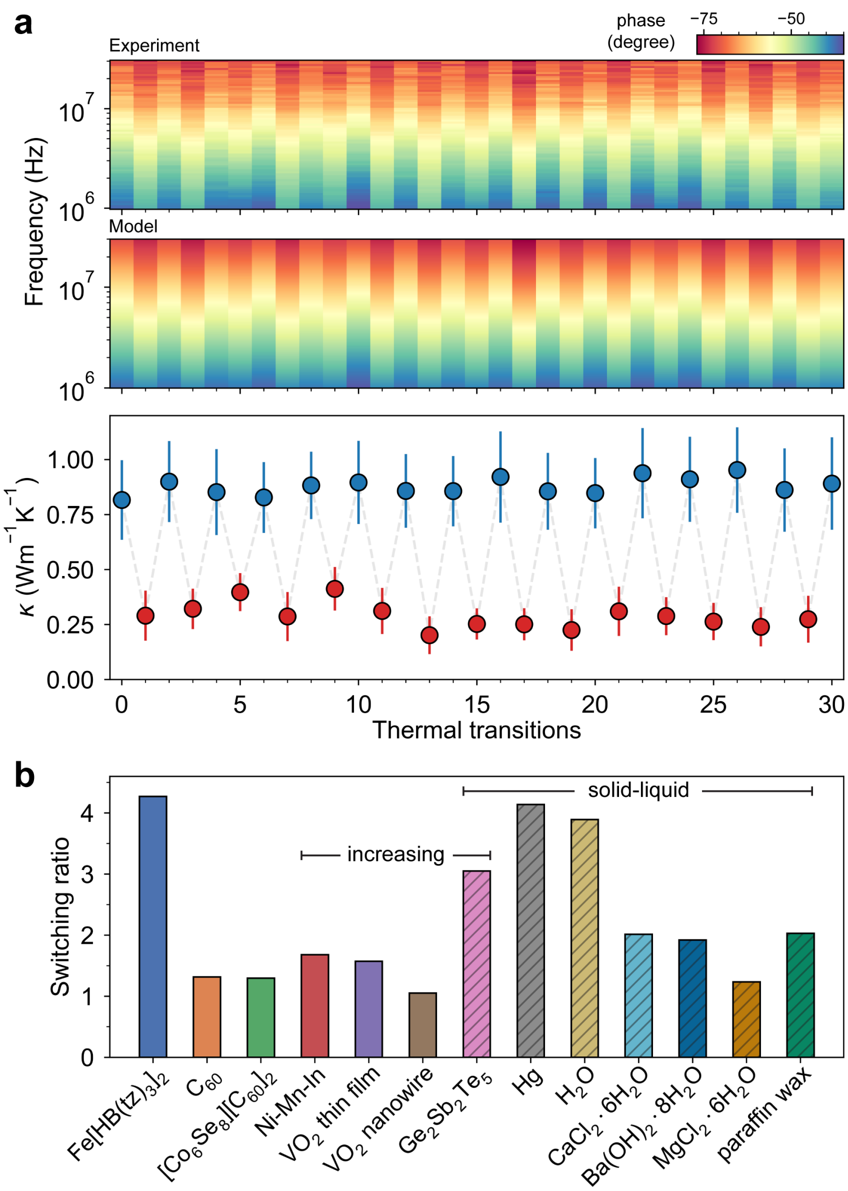

Fig. 2 | Reversible thermal conductivity switching in $Fe[HB(tz)_3]_2$. a, The phase lag of the thermoreflectance signal from FDTR measurements (top) and best fits from a Fourier heat conduction model (middle) are represented by colormaps for 30 thermal transitions between 303 K and 343 K. The thermal conductivity determined at 303 K (blue) and 343 K (red) within each cycle (bottom). **b**, The thermal conductivity switching ratios of representative solid-solid and solid-liquid phase-change materials are compared. All materials exhibit decreased thermal conductivity in their high-temperature phases, with the exception of the four materials indicated as "increasing".

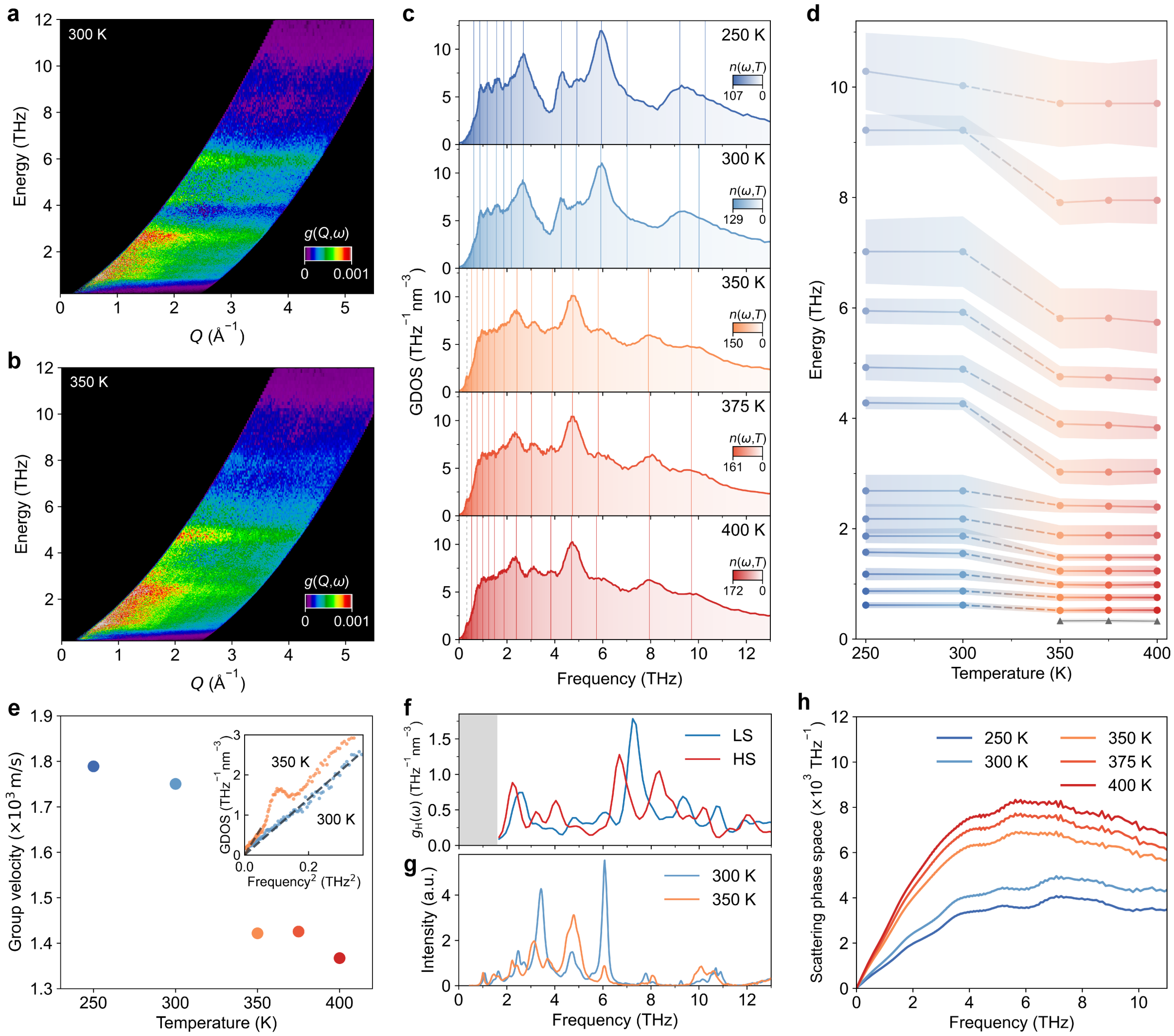

Fig. 3 | Phonon softening observed in inelastic neutron scattering and Raman scattering. a,**b**, The normalized inelastic neutron scattering function $g(Q,\omega)$ at a given momentum transfer and energy for the LS (**a**) and HS (**b**) phases of $Fe[HB(tz)_3]_2$. **c**, The generalized phonon density of states, GDOS(ω), for the LS phase at 250 K and 300 K and for the HS phase at 350 K, 375 K and 400 K. The solid lines correspond to optical phonon peaks from pseudo-Voigt fits, while the dashed lines in HS phases represent zero-field splitting-related excitations. The color gradient represents the Bose-Einstein distribution function $n(\omega,T)$ (the phonon occupation number), ranging from 0 to n (0.048 THz , T), with darker colors indicating higher occupation numbers. **d**, The peak positions of all optical phonon bands from pseudo-Voigt fits as a function of temperature. The shaded area represents the full width at half-maximum of each peak. Note that the narrow, lowest-energy peak emerging in the HS phase (dark gray) is due to the presence of unpaired electrons. **e**, Temperature-dependent phonon group velocity. The inset illustrates that the low-frequency GDOS scales with ω^2 and the scaling factor (inversely related to phonon group velocity) changes significantly when the spin state changes. **f**, Hydrogen-projected phonon density of states from density functional tight-binding calculations. Gray-shaded regions indicate imaginary phonon modes excluded from the comparison. **g**, Ultra-low-frequency Stokes Raman scattering intensity for the LS and HS phases. The Raman scattering intensity is normalized by the factor $\frac{n(\omega,T)+1}{\omega}$. **h**, Three-phonon scattering phase space—a measure of the number of possible energy-conserving phonon scattering events—as a function of frequency at different temperatures.

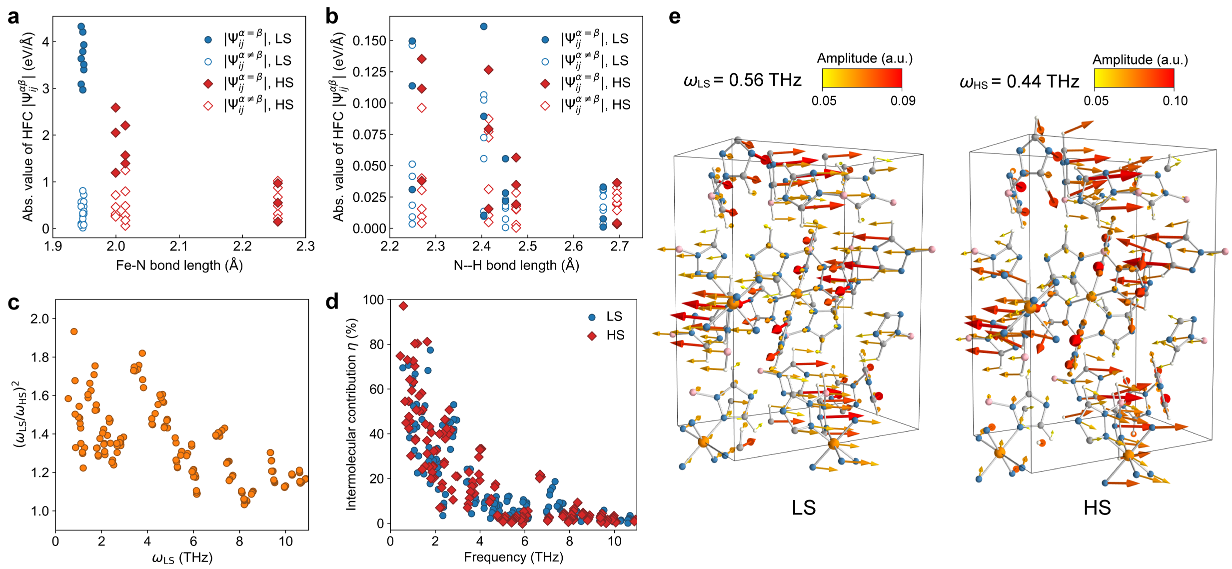

Fig. 4 | Contributions of intra- and intermolecular interactions to thermal transport. a,**b**, The intramolecular harmonic force constants of Fe–N bonds (**a**) and the intermolecular harmonic force constants of N--H hydrogen bonds (**b**). The filled and unfilled markers correspond to the harmonic force constants where atom i and atom j move along the same ($\alpha = \beta$) and different ($\alpha \neq \beta$) Cartesian axes, respectively. **c**, The ratio of the optical phonon frequencies in the LS and HS phases. **d**, The contribution of intermolecular vibrations to phonons in the LS and HS phases. **e**, The phonon polarization vectors in the unit cell of Fe[HB(tz)$_3$]$_2$ for the lowest-energy optical phonon mode with ω_{LS} = 0.56 THz in the LS phase and ω_{HS} = 0.44 THz in the HS phase. The color and length of the arrows reflect the amplitude of the polarization vector.

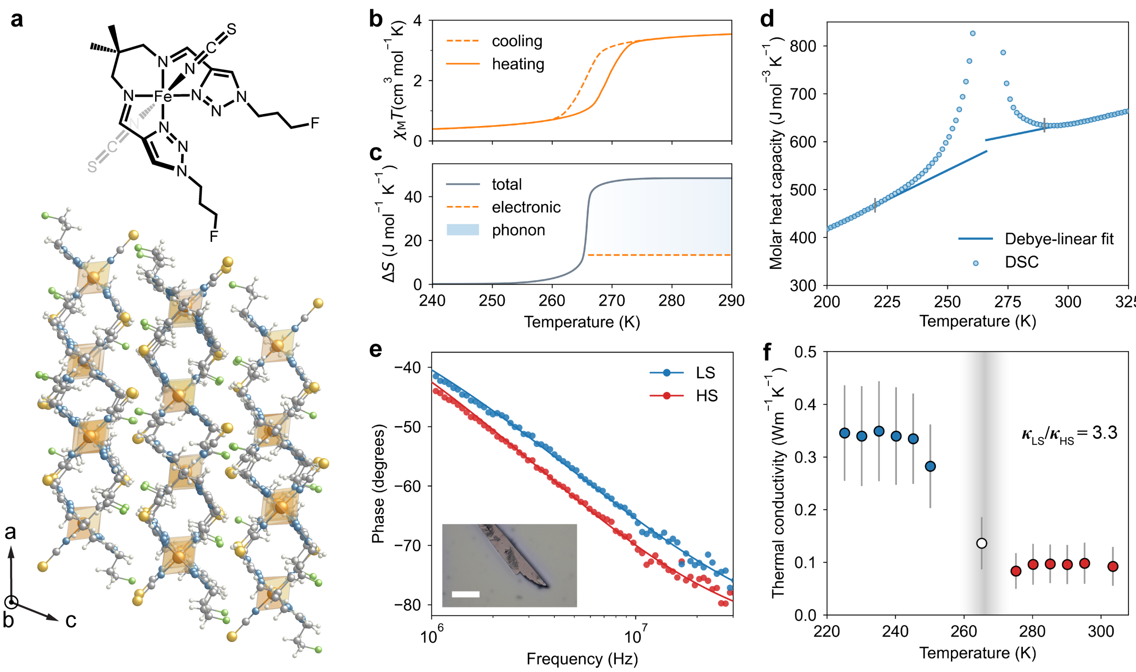

Fig. 5 | Generalizability of spin-crossover-driven thermal regulation. **a**, Molecular structure of Fe(Fpr-trz$_2$-dmpn)(NCS)$_2$ and crystal structure of the LS phase. Orange, grey, blue, white, yellow, and green spheres represent Fe, C, N, H, S, and F atoms, respectively. **b**, Singlet-to-quintet spin-crossover transition revealed by magnetic susceptibility measurements. **c**, Entropy change of the spin-crossover transition measured from DSC, with phonon entropy contributing more than 72% to the overall entropy change. **d**, Heat capacity of Fe(Fpr-trz$_2$-dmpn)(NCS)$_2$ from DSC measurements (circles) along with a fit that combines a Debye model with a linear-in-T term (lines). Temperatures within the phase-transition region (delineated by vertical grey bars) are omitted from the heat capacity model fitting. **e**, Phase lag of thermoreflectance from FDTR measurements (dots) and best fits (lines) in the LS (238 K, blue) and HS (273 K, red) phases. The inset shows an optical image of an Fe(Fpr-trz$_2$-dmpn)(NCS)$_2$ single crystal coated with a gold transducer layer. Scale bar, 100 μm. **f**, Thermal conductivity of the Fe(Fpr-trz$_2$-dmpn)(NCS)$_2$ single crystal in the LS (blue circles) and HS phases (red circles). Shaded region: 14 K window around T_{tr} = 266 K with phase coexistence.

Acknowledgements

We thank Catherine Badding for assistance with the heat capacity measurements and Svetlana Boriskina for helpful discussions. Neutron beam time was awarded at the Australian Nuclear Science and Technology Organisation under proposal P17369. This work was performed in part at the Harvard University Center for Nanoscale Systems (CNS), a member of the National Nanotechnology Coordinated Infrastructure Network (NNCI), which is supported by the National Science Foundation under NSF award number ECCS-2025158. Q.S. acknowledges the support from the Harvard Quantum Initiative.

Author contributions

J.A.M. and J.Se. developed the initial idea for this research, and J.A.M. supervised the project. Q.S. and J.Sh. conducted the FDTR measurements and performed the analysis. V.M.D. and J.D.B. grew the single crystals and conducted the SQUID measurements. Q.S., R.U., C.T., D.W.L. and R.D.M. contributed to sample preparation. Q.S. performed the phonon calculations and theoretical analysis and G.C. contributed to this analysis. H.K.K. performed the DFTB and DFT calculations. R.U., C.S. and D.Y. conducted the neutron scattering experiments. Q.S., R.U. and V.M.D. conducted the Raman scattering measurements. R.U. conducted the nanoindentation measurement. R.D.M. and R.U. performed DSC measurements. J.J.C., R.U., Y.M. and R.D.M. conducted heat capacity measurements. Q.S, Y.M. and R.U. developed the alloy transducer. Q.S., J.Se., and J.A.M. wrote the manuscript. All authors contributed to data analysis and editing the manuscript.

Competing interests

J.A.M, J.Se., R.D.M., J.D.B. and R.U. are inventors on a patent application related to this work held and submitted by Harvard University.

Data Availability Statement

Selected source data is provided with this paper, and further data is available from the corresponding author upon reasonable request.

Code Availability Statement

The data analysis code is available at https://github.com/qichensong/sco-thermal. Other relevant codes are available from the corresponding author upon reasonable request.